The influence of multi-body interaction on the hydrodynamic performance of a hexagon-type floating photovoltaic

Yan Li[1], Guoyan Li[1], Yiwen Cui[1], Wanru Deng[1,2*], Bin Wang[3], Haoran Li[1], Yiting Feng[1], Hang Meng[4]

[1] State Key Laboratory of Hydraulic Engineering Intelligent Construction and Operation, Tianjin Key Laboratory of Port and Ocean Engineering, School of Civil Engineering, Tianjin University, Tianjin, 300350, China

[2] Naval Architecture, Ocean and Marine Engineering Department, University of Strathclyde, Glasgow, United Kingdom

[3] Research Institute of Offshore Energy and Intelligent Construction, Tianjin University of Technology, Tianjin, 300384, China

[4] State Key Laboratory of Alternate Electrical Power System with Renewable Energy Sources, School of New Energy, North China Electric Power University, Beijing, 102206, China

Abstract

Clean energy development is an inevitable trend with the increasing demand for electricity. Among marine renewable energy sources, floating photovoltaic (FPV) is becoming a concern, which move to large-scale arrays progressively. Thus, it is necessary to understand the multi-body interaction effect. In this work, a multi-body FPV with four hexagon-type modules is adopted to investigate this phenomenon. Two models are established, including a multi-body model and a single-body model. Based on the composite hydrodynamic method that combines potential theory and the Morison formula, motion response and mooring load variations between two models are compared under combined wave and wind conditions. The results show that the multi-body interaction exhibits distinct characteristics for different modules and mooring lines. The motion becomes more significant when the multi-body model interaction is included, while the oscillations and maximum values of mooring tension decrease. Furthermore, we discuss the dynamic performance of the FPV under different wave parameters to explore the effect of environmental loads on the multi-body interaction.

Key words: Hexagon-type FPV; Multi-body model; Hydrodynamic performance; Dynamic response

* Corresponding author E-mail address: dengwanru@tju.edu.cn

1. Introduction

Climate change is a challenge for all of humanity. The development of renewable energy is becoming an important prescription for addressing the climate crisis and meeting the energy requirements [1]. Among renewable sources, solar energy, is a fast-growing clean energy with broad application prospects [2]. In order to convert solar energy into electricity, devices such as photovoltaics need to be utilized.

Among all solar power generators, offshore photovoltaics is one of the most promising technologies. The trend towards large-scale, arrayed photovoltaic systems is inevitable. In this regard, offshore photovoltaics benefit from more abundant sunlight and broader available space compared with onshore photovoltaics, reducing the impact and necessity for land resources and enhancing the economic feasibility of the technology [3]. Hence, increasingly floating photovoltaic (FPV) projects have been implemented all over the world in recent years [4,5]. Despite the growing momentum of FPV development, the technology level of offshore FPVs remains relatively low due to the harsh marine environment [6].

Therefore, several significant topics on hydrodynamic have attracted widespread attention and further research, such as the dynamic performance of mooring lines and connections, the analysis of environment loads on FPVs, and the development of model test methods.

Designing mooring systems for FPV is one of the greatest challenges. FPV systems typically operate in lakes or coastal areas, requiring the mooring system to be arranged in shallow water and to provide sufficient station-keeping capability for the platform. Extensive tidal variations also pose a significant challenge. Therefore, sensitivity analyses have been conducted using various mooring parameters and arrangements in the design of mooring systems. Du et al. assessed the performance of six distinct mooring configurations in different tidal levels. It is suggested that buoys or clumps can optimize the stability and resilience of the FPV arrays [7]. Song et al. compared the taut and catenary mooring systems and analyzed the effect of line nominal diameter on structural response [8].

It is also essential to study the effect of the connection for multi-module systems. In FPVs, numerous floaters are interconnected to form a whole system that achieves the target capacity. Hereby, the connections between different modulus significantly influence the overall kinematic performance. Moreover, the connector failure may lead to tremendous losses, hence it is crucial to evaluate the security and analyze the effect of the connection. Most research in this area focuses on analyzing the effects of different connection forms and optimizing the design. Song et al. conducted a connector boundary condition sensitivity test for a FPV system with vertical cylinders. They found

an unexpected dynamic response in the hinged connector case [9]. Yan et al. compared different connection boundary conditions and observed that the hinged joint generates additional moments, thereby increasing the excitation load on the platform [10]. Some scholars used ball joints, rubber rings, and their combinations to amalgamate modules, studying the influence of these connectors on motion, tension and air gap [11].

How to accurately evaluate the effect of hydrodynamic loads on FPVs is also a crucial issue. The complexity and variability of the marine environment not only weaken the power generation performance [12,13], but also pose significant safety threats to the FPV system [14]. Thus, to prevent equipment mismatch from damaging, FPV systems require to withstand the marine cyclic loads and survive extreme conditions [15]. The marine environment poses substantial challenges to platform performance, involving the complex task considering the combined wind, waves, and currents. Therefore, analyzing the effects of various sea state parameters is necessary to optimize the mooring system. Wang et al. proposed a star-type FPV and investigated the influence of different wave parameters on the dynamic response of mooring and connector systems. The results showed that mooring tension is sensitive to wave parameters [16]. A methodology to assess the dynamic response and the structural performance of FPV has been presented by Ruben et al.. They proved that wind forces primarily influence surge and sway, while wave forces determine other motions [17]. The direction of the wave loads also affect the hydrodynamic response of FPV. Some studies have shown that it is preferable for transverse direction to align with wave direction [18].

Furthermore, model tests were conducted to validate the numerical simulation. Jiang et al. performed a model test for a novel FPV concept under regular and irregular waves, verifying the excellent performance of the system [19]. Laboratory tests were carried out by Dai et al. to assess the structural performance of FPV and inter-modular connectors. The design adequacy is satisfactory [20].

Nevertheless, there are few studies focusing on the multi-body problem for large-scale FPV arrays. Unlike typical floating offshore platforms, FPVs are often designed as arrays of multiple floating bodies, necessitating in-depth investigation of the coupled interaction between platforms when studying aforementioned problems. From this perspective, we established FPV-mooring coupled models with and without considering multi-body effect to assess the difference in hydrodynamic performance. A floating photovoltaic system consisting of four hexagon-type modules is proposed to conduct the research. A hybrid model is established by combining 3D potential-theory diffracting panels and Morison elements. On this basis, a quasi-static catenary model simulating the mooring lines is adopted to couple with the hydrodynamic model for dynamic response analysis in the time domain.

The remainder of this paper is organized as follows. In Section 2, the system and modeling are described firstly, including single module configuration, as well as the connectors, the fenders and the mooring lines. Afterwards, brief descriptions of the numerical methodology are introduced in Section 3. In Section 4, we conducted a validation to verify the numerical model and methodology. In Section 5, the simulation results are displayed and analyzed. We studied the interaction between modules and the effects of environmental parameters on it. Finally, Section 6 draws a conclusion and give a summary of future work.

2. System description

Fig. 1 displays the sketch of a single FPV module, and Table 1 provides the structural parameters. Borrowing from the honeycomb structure, individual module is designed as a regular hexagon. The primary principle is that perimeter of a hexagon is minimized when there are no gaps or overlaps covering the entire plane. Consequently, the hexagon-type FPV not only increases the space utilization, but also saves material. The FPV system consists of four hexagonal floaters with an edge length of 26 m. Each floater is composed of several uniformly arranged cylindrical pontoons and their corresponding tube-type frames and braces. A total of 270 photovoltaic panels are arranged in a single module, each 3 m long and 2 m. The installed capacity of a singular module can reach about 0.35 MW. A Cartesian coordinate system is defined for the whole FPV system. Its origin is located on the Mean Stillwater Line plane with the z-axis pointing upwards.

To release the tidal effect on water depth, a catenary mooring system is adopted around the photovoltaic arrays, consisting of 20 studless chains (see Table 2). Additionally, the floaters are interconnected to each other by flexible connectors as well as fenders for crashworthiness. The layout of the FPV system, including mooring system, connectors and fenders, is shown in Fig. 2. The modeling methods for these flexible connections are introduced in section 3.
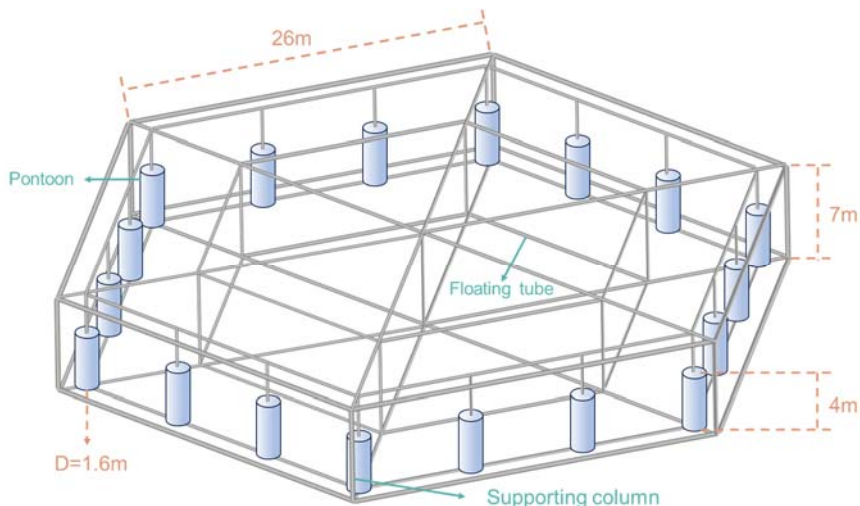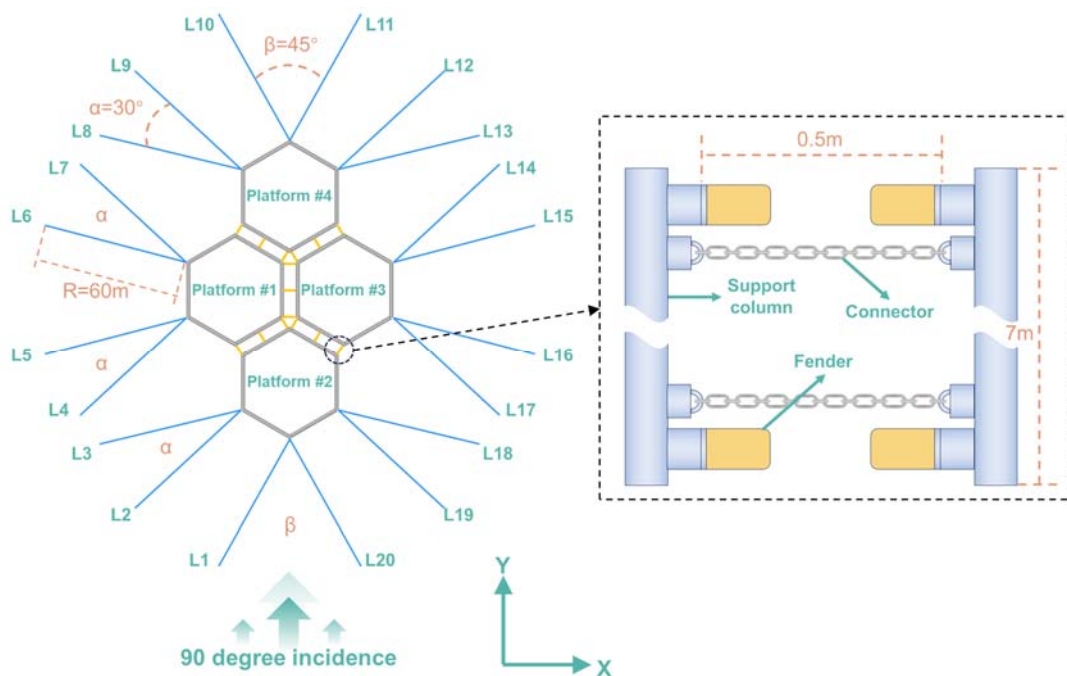
4

Fig. 1 The sketch of the FPV module

Fig. 2 The layout of the FPV system

Table 1 Parameters of the FPV module.

Parameters	Values	Unit
Pontoon		
Diameter	1.6	m
Height	4	m
Steel frame		
Diameter of support columns	0.205	m
Diameter of floating tubes	0.11	m
Platform		
Total weight	113750	kg

Draft	3	m
Dimensions	45.033×52×7	m
Moment of inertia I_{xx}	36855000	kg·m^2
Moment of inertia I_{yy}	29120000	kg·m^2
Moment of inertia I_{zz}	45500000	kg·m^2

Table 2 Parameters of the mooring lines and connectors.

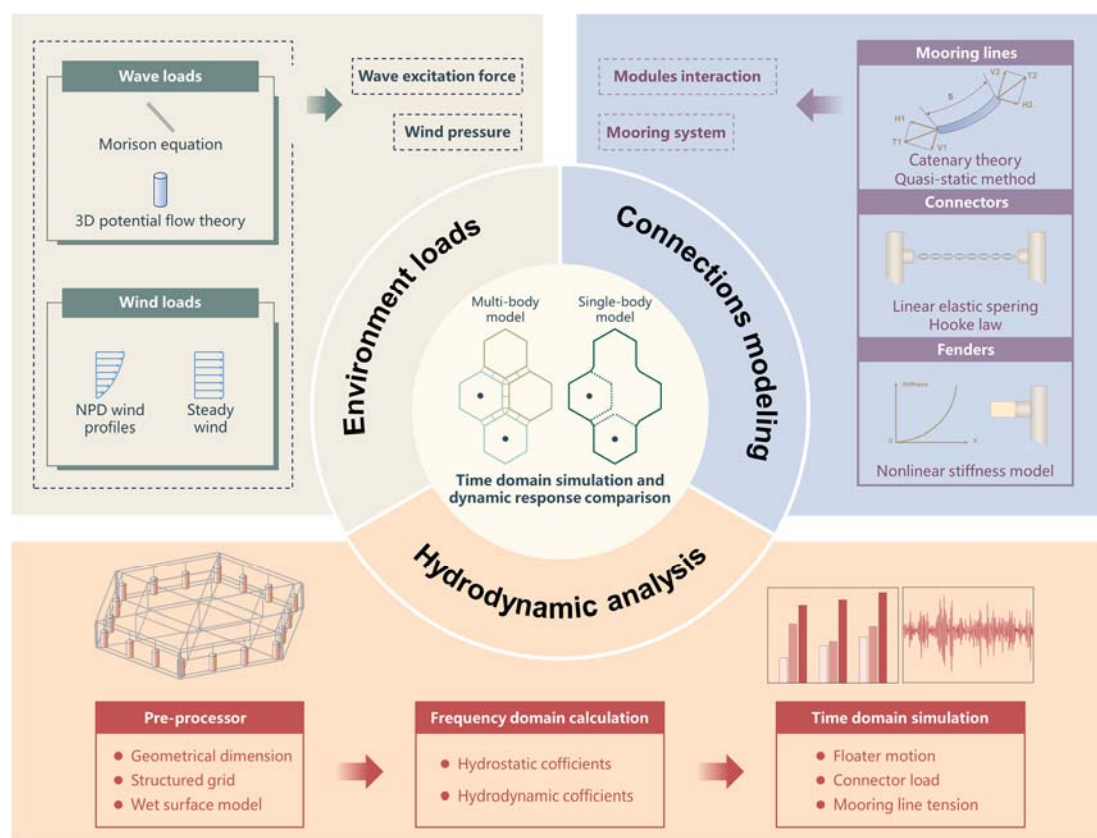| Parameters	Values	Unit
Mooring line		
Outer diameter	0.06	m
Weight in air	26	kg/m
Axial stiffness	1.05E8	N
Minimum breaking tension	1.1E6	N
Connector		
Axial stiffness	1.96E6	N
Unstretched length	0.5	m

3. Methodology

Fig. 3 The methodology overview

We establish a mooring-platform-connector-fender coupled hydrodynamic model

as the multi-body model. In contrast, the single-body model treats the four modules as structural components forming a larger platform. Although the two models have similar boundary conditions for the modular connections, the single-body model disregards the multi-body effect between modules when calculating the hydrodynamic coefficients and solving the equations of motion in the time domain. Detailed equations can be seen in this section below.

In general, a numerical time domain model of FPV includes environmental loads, connections modeling and hydrodynamic analysis of the platforms. It should be noted that current forces have minimal contribution on the total load [14], hence it is neglected in our work to improve computational efficiency. The methodology overview is shown in Fig. 3.

3.1 Wind load

Wind load is the governing environmental load in onshore or lake solar system. In the irregular wave conditions, we adopted the Norwegian Petroleum Directorate (NPD) wind profiles to define the mean one-hour wind speed at height H,

$$\bar{V}_H = \bar{V}_{10}[1 + C\ln(\frac{H}{10})],\qquad(1)$$

where $C = 0.0573\sqrt{1 + 0.15\bar{V}_{10}}$, $\bar{V}_{10}$ is the mean velocity in at 10 m above mean water surface. On the other hand, when the steady wind is adopted in the regular wave conditions, the wind speed is uniform with height.

The wind load on the floater is considered as constant forces, which can be expressed by following formula,

$$\boldsymbol{F}_{wind} = \frac{1}{2}\rho \boldsymbol{V}_w^2 A_w C_d C_s,\qquad(2)$$

where ρ is the fluid density, A_w the area exposed to the wind, $\boldsymbol{V}_w$ is the wind velocity, C_s is the sheltering coefficient and C_d is the drag coefficient. The corresponding wind load parameters are adopted from the Maria's publication [14].

3.2 Wave simulation

JONSWAP spectrum is a formulated wave spectra to define the irregular wave, which can consider the imbalance of energy flow. The spectral at a frequency can be expressed by,

$$S(\omega) = \frac{ag^2\gamma^a}{\omega^5}exp(-\frac{5\omega_p^4}{4\omega^4}),\qquad(3)$$

where ω_p is the peak frequency, γ is the peakedness parameter, a is a constant related to γ, ω_p, and significant wave height.

The simulation of regular waves is convenient and efficient to better understand how wave parameters affect the motion response. This paper adopts the second-order Stokes wave theory to simulate the regular wave. Assuming that the ratio of wave amplitude to wavelength is a smallness perturbation parameter, the wave elevation $\eta(X, Y; t)$ at location of (X, Y, Z) can be expressed by adopting the perturbation method,

$$
\begin{aligned}
\eta(X,Y;t) &= \eta^{(1)}(X,Y;t) + \eta^{(2)}(X,Y;t) \\
&= a_w e^{i(-wt+kX\cos\theta+kY\sin\theta+a)} \\
&\quad + \frac{1}{4}ka_w^2 \frac{\cosh(kh_d)}{\sinh^3(kh_d)}[2+\cosh(2kh_d)]e^{2i(-wt+kX\cos\theta+kY\sin\theta+a)}
\end{aligned}
\tag{4}
$$

where a_w is the wave amplitude, w is the wave frequency, k is the wave number, θ is the wave incident direction, a is the wave phase, h_d is the water depth.

3.3 Morison's equation

When the cross sectional diameter D of the members is small compared to the wavelength L (i.e. $D/L<0.2$), it is assumed that they have no effect on the wave particle motion, and the wave action mainly composed of viscosity effect and added mass effect [21]. The Morison's equation is employed to model these components of FPV by Morison elements. Specifically, this algorithm is adopted to calculate the hydrodynamic loads on the steel frame of the FPV. The wave loads acting on these slender structures can be calculated by the following equation,

$$
\begin{aligned}
d\boldsymbol{F} &= d\boldsymbol{F}_d + d\boldsymbol{F}_I \\
&= \frac{1}{2}\rho DC_d |\boldsymbol{u}_f - \boldsymbol{u}_s|(\boldsymbol{u}_f - \boldsymbol{u}_s) + \rho AC_m\dot{\boldsymbol{u}}_f - \rho A(C_m-1)\dot{\boldsymbol{u}}_s
\end{aligned}
\tag{5}
$$

where $\boldsymbol{F}_d$ and $\boldsymbol{F}_I$ is the drag and inertial forces, D is the characteristic drag diameter, u_f is the transverse directional wave particle velocity, $\boldsymbol{u}_s$ is the transverse directional structure velocity, C_m is the inertia coefficient, A is the cross-sectional area.

As seen from Eq. (5), the drag force component in the Morison's equation is nonlinearly related to the fluid particle velocity. To simplify calculations, a statistical method is employed to linearize the quadratic drag force term. The linearized drag force at a cross section of a tube is expressed as,

$$
d\boldsymbol{F}_{drag} = \frac{1}{2}\rho DC_d\alpha u_{rms}(\boldsymbol{u}_f - \boldsymbol{u}_s),
\tag{6}
$$

where α is an equivalent linear term replaced $|\boldsymbol{u}_f\text{-}\boldsymbol{u}_s|$. u_{rms} is the root mean square of transverse directional relative velocity at that location.

3.4 Three-dimensional potential flow theory with hydrodynamic interaction

Three-dimensional potential flow theory is a classic method to calculate the wave excitation forces on the diffracting panel, such as the floating pontoons on the FPVs. By assuming the fluid ideal such that there exists a velocity potential function $\varphi(\vec{X})$ surrounding a floating body. It can be separated into contributions from the radiation, the incident and the diffraction wave. Hence the first-order wave force is calculated by,

$$F_j = F_{ij} + F_{dj} + \sum_{k=1}^{6} F_{rjk} x_k \ (j = 1, 6), \tag{7}$$

where F_{ij} is the j-th incident force, F_{dj} is the j-th diffraction force, F_{rjk} is the j-th radiation force under the k-th degree of body motion x_k.

Particularly, hydrodynamic interaction can be taken into account in the FPV multiple platform analysis. In this case, amendment is required on the radiation as well as the diffraction forces. The total unsteady potential can be expressed as a preposition,

$$\varphi(\vec{X})e^{-i\omega t} = [(\varphi_I + \varphi_d) + \sum_{m=1}^{N}\sum_{j=1}^{6} \varphi_{rjm} x_{jm}]e^{-i\omega t}, \tag{8}$$

where φ_I is the first order incident wave potential and φ_d is the diffraction wave potential. x_{jm} is the m-th structure motion amplitude of the j-th degree of freedom. φ_{rjm} is the radiation potential due to the j-th motion of the m-th structure while other structures keep stationary. N is the total number of platforms.

When the velocity potentials are known, the hydrodynamic pressure distribution may be calculated by using the linearized Bernoulli's equation. Furthermore, the various fluid forces can be calculated by integrating the pressure over the wetted surface of the body. Employing this method, the first order hydrodynamic force can be written as following,

$$F_{jm} = [(F_{Ijm} + F_{djm}) + \sum_{n=1}^{N}\sum_{m=1}^{N}\sum_{k=1}^{6} F_{rjm,kn} x_{km}] \ (m \neq n, j = 1, 6), \tag{9}$$

where F_{Ijm} is the j-th Froude-krylov force of m-th platform, F_{djm} is the j-th diffraction force of m-th platform. $F_{rjm,kn}$ is the j-th radiation force correspond to the k-th motion modes between the m-th and the n-th platform. x_{km} is the k-th motion modes of the m-th platform.

3.5 Quasi-Static catenary method for mooring line

This paper adopted Quai-Static method considering the elastic deformation correction to establish the catenary mooring line model.
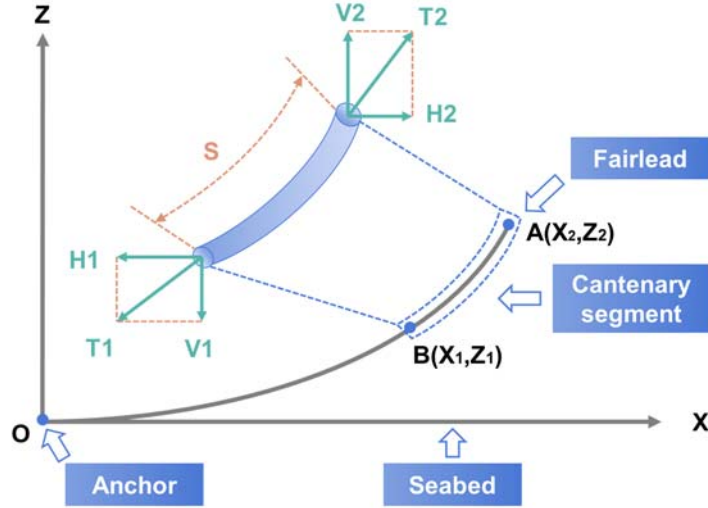
Fig. 4 The model of catenary theory

As seen in Fig. 4, for a uniform catenary with axial linear elasticity, Node #A represents the fairlead and Node #B is the bottom end of a catenary segment. Assuming that the slope of the seabed is zero at the anchor point, the catenary equations are expressed in a local axis system O-XYZ, where the X-axis is parallel to the seabed, and the Z-axis is oriented vertically upward. The positions and the tension components of Node #A can be written as,

$$H_2 = AE\sqrt{(\frac{T_2}{AE}+1)^2 - \frac{2wZ_2}{AE}} - AE ,\tag{10}$$

$$X_2 = \frac{H_2}{w}\sinh^{-1}(\frac{wL}{H_2}) + \frac{H_2 L}{AE} ,\tag{11}$$

$$V_2 = wL ,\tag{12}$$

$$T_2 = \sqrt{H_2^2 + V_2^2} ,\tag{13}$$

where X_2 and Z_2 are the X and Z coordinates of Node #A, X_1 and Z_1 are the X and Z coordinates of Node #B. T_2, H_2 and V_2 are the tension and its components at Node #A. likewise, T_1, H_1 and V_1 are the tension and its components at Node #B. L is the unstretched length from the origin to Node #A, w and EA are respectively the wet weight and stiffness per unit length of the line.

Suppose that the unstretched length of mooring segment is S, the coordinates and the tension components of Node #B are given by,

$$X_1 = \frac{H}{w}\ln\frac{V_2 + T_2}{V_1 + T_1} + \frac{HS}{AE} ,\tag{14}$$

$$Z_I = \frac{V_2 + V_I}{T_2 + T_I} S + S \frac{V_2 + V_I}{2AE}, \tag{15}$$

$$H_1 = H_2, \tag{16}$$

$$V_1 = V_2 - wS, \tag{17}$$

$$T_I = \sqrt{H_1^2 + T_1^2}. \tag{18}$$

3.6 Connectors and fenders

Linear elastic line elements are selected to model the connectors, which are assumed to be weightless and uncompressed. The linear stiffness k_0=1.96E6 N/m. Fenders are utilized for crashworthiness, simulated by unstretched spring elements with nonlinear stiffness. The magnitude of the fender's axis-directional compression force is defined as,

$$T = \begin{cases} k_1 \Delta L + k_2 (\Delta L)^2 + k_3 (\Delta L)^3 & if \Delta L > 0 \\ 0 & if \Delta L \le 0 \end{cases} \tag{19}$$

$$\Delta L = L_0 - L_a \tag{20}$$

where k_1=240000 N/m, k_2=-81660 N/m^2, k_3=192600 N/m^3. L_0 is the initial size of the fender, L_a is the actual distance between the two contacting points of the fender.

3.7 Equation of motion in time domain

The frequency components in irregular wave are diverse and complex. Consequently, the added mass and potential flow damping calculated in frequency domain are transformed into the form of motion hysteresis function by convolution integral. In the single-body model, the governing equation is written in time domain as,

$$[M + m(\infty)] \times \ddot{\vec{x}} + \int R(t - \tau) d\tau \times \dot{\vec{x}} + K \times \vec{x} = \vec{F}, \tag{21}$$

where [M] is the 6×6 structure mass sub-matrix. [m] is the frequency-dependent added mass sub-matrix. [R(τ)] is the hysteresis function. [K] is the hydrostatic restoring sub-matrix. [x] is the displacement vector of platforms, and [F] is the exciting forces vector, which includes the wave-excited force, drift force, wind force and restoring force provided by mooring lines. The current loads were not taken into account in our work.

Considering the effect of multi-body hydrodynamic coupling on the diffraction and radiation potentials, the equation above can be modified as follows [22],

$$\begin{bmatrix} M_1 + m_{1,1}^a(\infty) & \cdots & m_{1,N}^a(\infty) \\ \vdots & \cdots & \vdots \\ m_{N,1}^a(\infty) & \cdots & M_N + m_{N,N}^a(\infty) \end{bmatrix} \begin{bmatrix} \ddot{\vec{x}}_1 \\ \vdots \\ \ddot{\vec{x}}_N \end{bmatrix}$$

$$+ \begin{bmatrix} \int R_{1,1}(t-\tau)d\tau & \cdots & \int R_{1,N}(t-\tau)d\tau \\ \vdots & \cdots & \vdots \\ \int R_{N,1}(t-\tau)d\tau & \cdots & \int R_{N,N}(t-\tau)d\tau \end{bmatrix} \begin{bmatrix} \dot{\vec{x}}_1 \\ \vdots \\ \dot{\vec{x}}_N \end{bmatrix}. \qquad (22)$$

$$+ \begin{bmatrix} K_{1,1} & & \\ & \ddots & \\ & & K_{N,N} \end{bmatrix} \begin{bmatrix} \vec{x}_1 \\ \vdots \\ \vec{x}_N \end{bmatrix} = \begin{bmatrix} \vec{F}_1 \\ \vdots \\ \vec{F}_N \end{bmatrix}$$

Due to the increase in the bodies numbers when considering the multi-body effect, the matrix dimension is broadened. The subscript represents the body number. *N=4* in this paper.

4. Validation

To validate our method, we conduct frequency and time domain simulations respectively. Firstly, the hydrodynamic analysis is carried out to validate our hydrodynamic algorithm. A star-type floating photovoltaic model proposed by Wang et al. [16] is adopted to perform this validation work. The numerical model is shown in Fig. 5 (a). The motion Response Amplitude Operators (RAOs) were calculated for wave period ranging from 2 s to 25 s with incident wave at 0 deg. The comparison results are shown in Fig. 5 (b) and (c). It can be observed that our results are generally in parallel with Wang et al., particularly in terms of the motion natural period. The slight difference in pitch and roll amplitudes mainly originate from the distinction of artificially added damping, which approximates viscous damping.

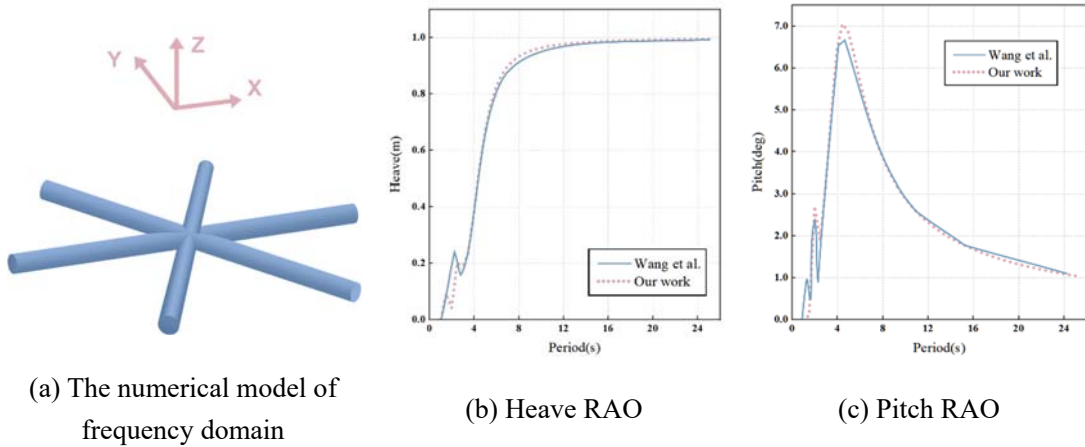| (a) The numerical model of frequency domain | (b) Heave RAO | (c) Pitch RAO |

Fig. 5 The frequency domain validation

Furthermore, time domain simulations are carried out under the same conditions

as Ji et al. [11]. The fully coupled multi-body algorithm is adopted to perform the validation work, and the corresponding model established is shown in Fig. 6 (a). We compare the maximum values of mooring line tension under different wave directions, and the results are shown in Fig. 6 (b) and (c). It could be found that our results agree well with those of Ji et al., confirming the validity and accuracy of our model and methods.
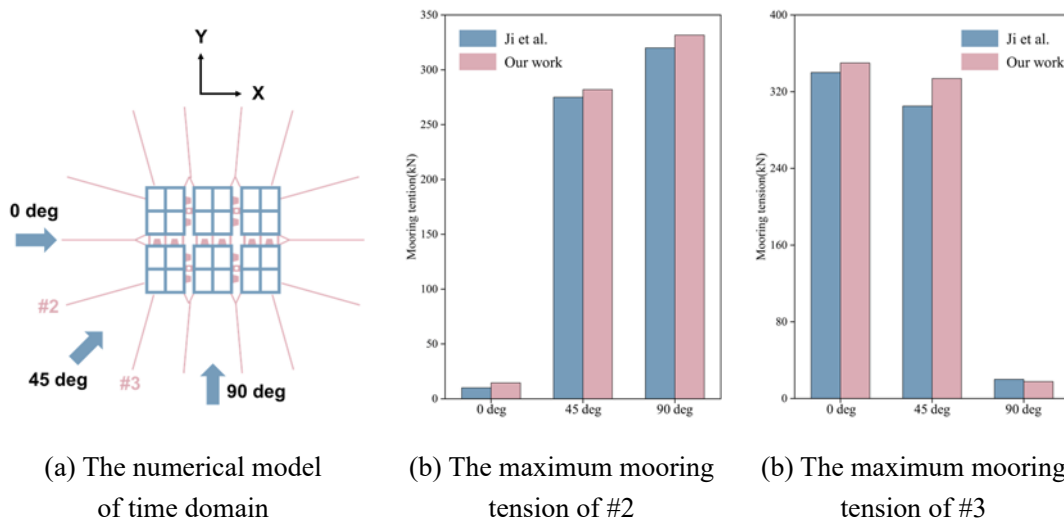

| (a) The numerical model of time domain | (b) The maximum mooring tension of #2 | (b) The maximum mooring tension of #3 |

Fig. 6 The time domain validation

5. Results and discussions

In this section, the multi-body and single-body models are established to analyze the FPV dynamic response under combined wave-wind conditions. Irregular wave simulations are carried out to study the influence of the multi-body effect, while regular wave simulations are conducted to investigate the variation of the influence under different environment loads. The main research content is shown in Fig. 7.
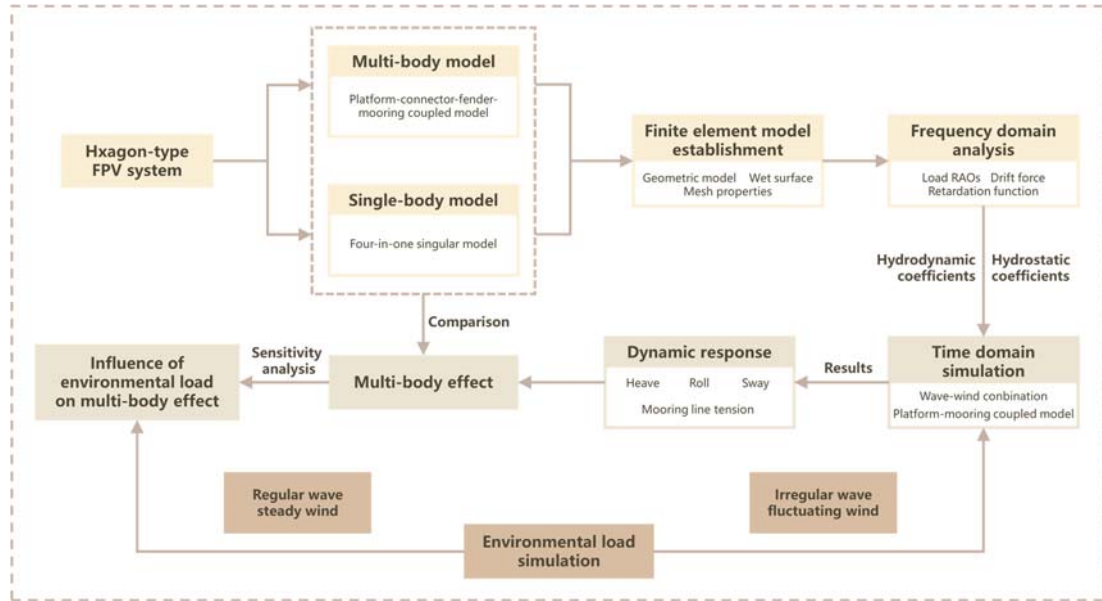
Fig. 7 The research content

5.1 Free decay tests

Before conducting the investigation, it is necessary to analyze the natural frequencies of the FPV module, which can deepen the understanding of the platform hydrodynamic and facilitate the study of frequency components in subsequent subsections. Hereby numerical free decay simulations of heave and roll is performed with a single module. Additionally, free decay of sway is simulated with platform #2 in multi-body model to consider the mooring line stiffness. The time histories are shown in Fig. 8. Simulation results, present that the natural periods of heave, roll and sway are 3.64 s, 3.97 s and 92.38 s, respectively. It is evident that the heave and roll natural periods of this FPV system are lower than those of common offshore platforms because of its smaller mass and added mass, while the sway natural period is higher due to the smaller stiffness of the catenary mooring lines.
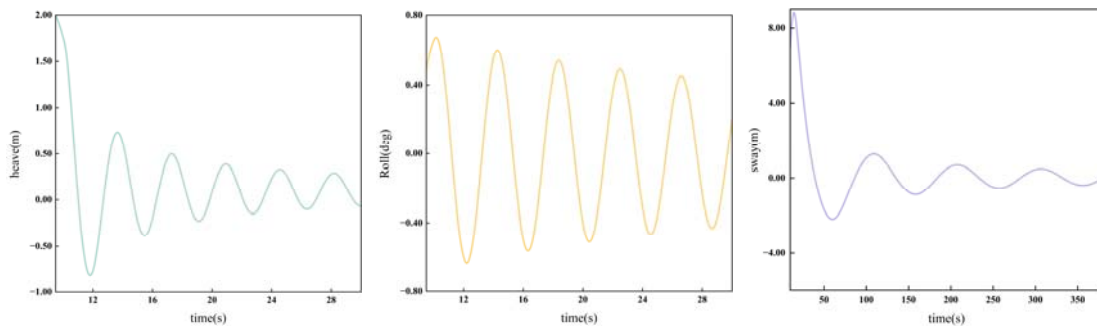
(a) Heave   (b) Roll   (c) Sway

Fig. 8 The heave, roll and sway free decay time history of singular module

5.2 Multi-body interaction effect

Maintaining a sufficient air gap is significant for keeping the FPV system away from green water and protecting the power generation equipment. The air gap primarily depends on swing and vertical translation. Therefore, heave and roll responses are key targets to study given the environment load incident angle of 90 deg. Besides, sway is the most critical factor for the safety of the mooring system and requires careful consideration. Thus, in this subsection, we focus on the motions of heave, roll, and sway. Furthermore, we discuss how mooring loads are influenced by multi-body interactions.

The details of the once-in-a-century environmental parameters adopted are listed in Table 3. The time-domain simulation chooses the most dangerous scenario where wind and waves are aligned. By comparing the results of the four-body hydrodynamic model, we analyze the effects of multi-body interactions on the dynamic response of the FPV. Considering the symmetry and the position of the head wave, platforms #1 and #2 are selected for the multi-body simulation analysis. In the single-body model, the gravity center positions of these two modules are set as reference points to analyze the motion responses.

Table 3 Parameters of environment condition.

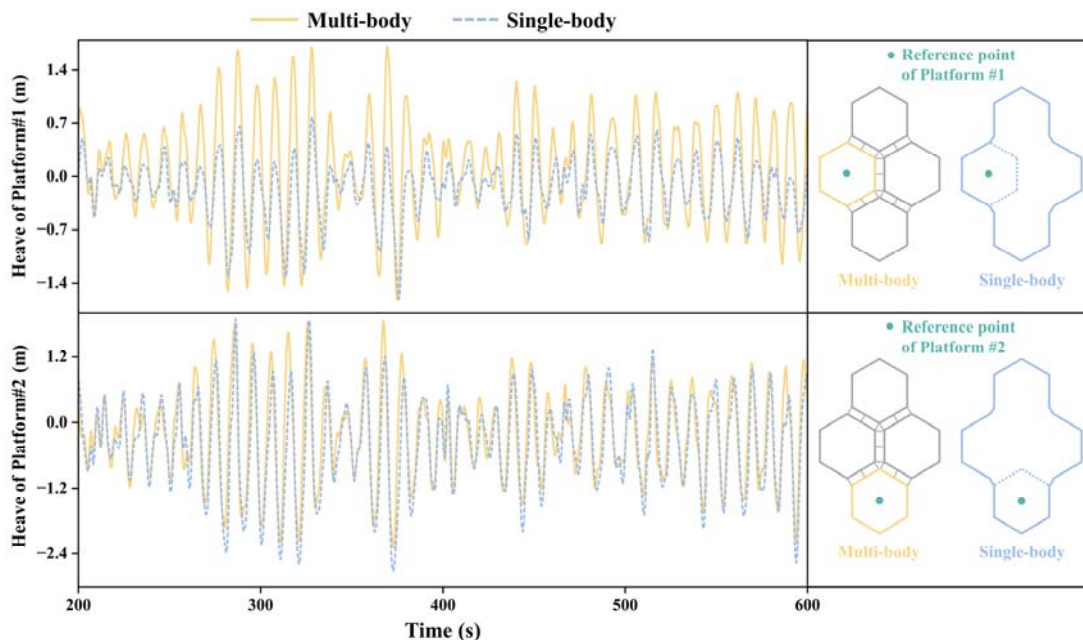| Parameters	Values	Unit
Wind spectrum	NPD	-
Wind speed	30	m/s
Wave spectrum	JONSWAP	-
Significant wave height	6	m
Peaked period	10	s
Peakedness parameter	3.3	-
Inflow direction	90	deg

5.2.1 Heave motion

Fig. 9 Heave time histories of Platform #1 and #2 with or without multi-body interaction

Fig. 9 shows the heave time histories of Platform #1 and #2 with and without multi-body interaction. It can be observed that the effect of multi-body interaction on different platforms varies considerably. Among them, the heave of Platform #1 is more sensitive to the multi-body interaction, with a more significant oscillation and an increase of 121.4% in the maximum value. Conversely, the heave of Platform #2 changes slightly under the multi-body effect. The maximum heave varies by only 1.7% compared to the single-body model, indicating that simulation with the single-body model still provides a relatively accurate prediction of the heave response of Platform #2.

The difference in heave response between Platform #1 and Platform #2 can be mainly attributed to connectors and fenders among floaters. For Platform #1, the connectors in the single-body model are rigid instead of flexible, and the constraints are significantly strengthened, so that the vertical equilibrium position is much closer to that of Platform #2, and the heave amplitude is substantially reduced. Platform #2, however, is at the forefront of the wave side, where Line #1 (L1) and Line #2 (L2) are fully tensioned most of the time. At this point, mooring lines have a superior impact on the heave motion. As a result, the heave response of Platform #2 varies inconspicuous with or without multi-body interaction.
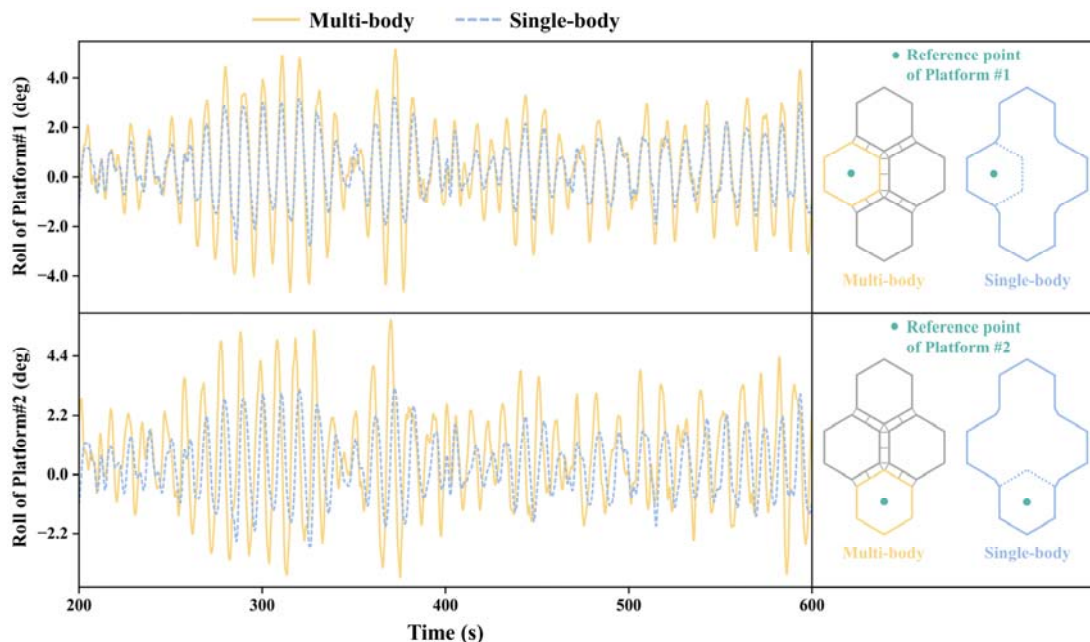
5.2.2 Roll motion

Fig. 10 Roll time histories of Platform #1 and #2 with or without multi-body interaction

Fig. 10 plots the roll time histories of Platform #1 and #2 with and without multi-body interaction. Similar influences are produced on the roll motion response of the two platforms between the multi-body model and the single-body model. By comparing the two models, we can find that the mean roll of the modules changes slightly, while the maximum response reaches 5.8 deg in the multi-body model, augmented by 77.3%. This indicates that multi-body interaction has a minor impact on the low-frequency response of roll but amplifies fluctuations in the wave-frequency response. It can be explained that the four platforms exhibit identical roll responses in the single-body model due to the rigid constraints, where the connectors can be regarded as beams with infinite stiffness. In contrast, during multi-body time domain analysis, the roll restoring moments provided by the connectors are reduced, thus the roll peaks increase in both positive and negative directions.

Similar to the heave response, amplitude variations primarily occur near the peak value. This suggests that the more significant the roll, the more pronounced the difference between the two models. Besides, from the roll time history of Platform #2, we see that there is a phase difference between the two models, indicating that the roll response lags behind when the multi-body effect is not considered.
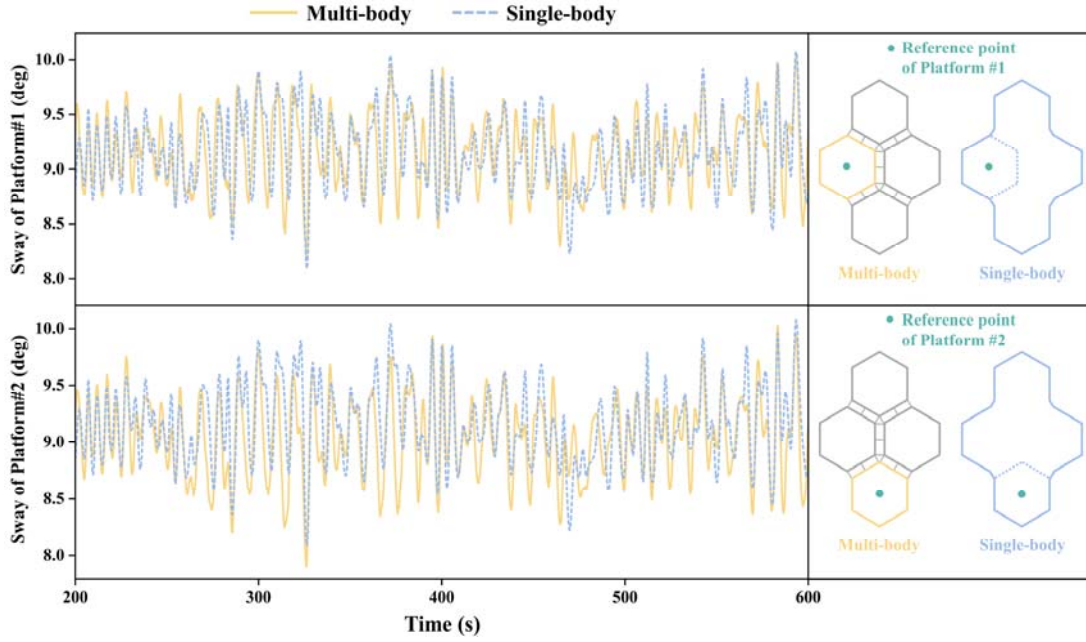
5.2.3 Sway motion

Fig. 11 Sway time histories of Platform #1 and #2 with or without multi-body interaction

The sway of Platform #1 and #2, with and without multi-body interaction, are shown in Fig. 11. The time histories reveal that the multi-body interaction influence on the sway is similar for the two platforms. Slight variations in the sway can be observed between the multi-body model and the single-body model, with less than a 1% difference in the mean and maximum values. This can be attributed to the comparable added mass in sway and identical external constraints, which are the main factors affecting motion in the horizontal plane. The local sway minimum values of the multi-body model are generally smaller due to the broader range of motion between platforms allowed by the flexible connectors. This effect is more evident on platform #2 owing to the higher mooring restoring forces.

5.2.4 Mooring line tension

As a coupled system, changes in motion will affect the mooring performance. In this subsection, we study the difference between the mooring system in the multi-body model and the single-body model. To express the difference clearly, we define the variation as follow,

$$V_t = (T_m - T_s) / T_s ,$$ (23)

where T_m is the tension in the multi-body model, T_s is the tension in the single-body model, V_t is the variation.

Table 4 Statistic of mooring tension in multi-body model

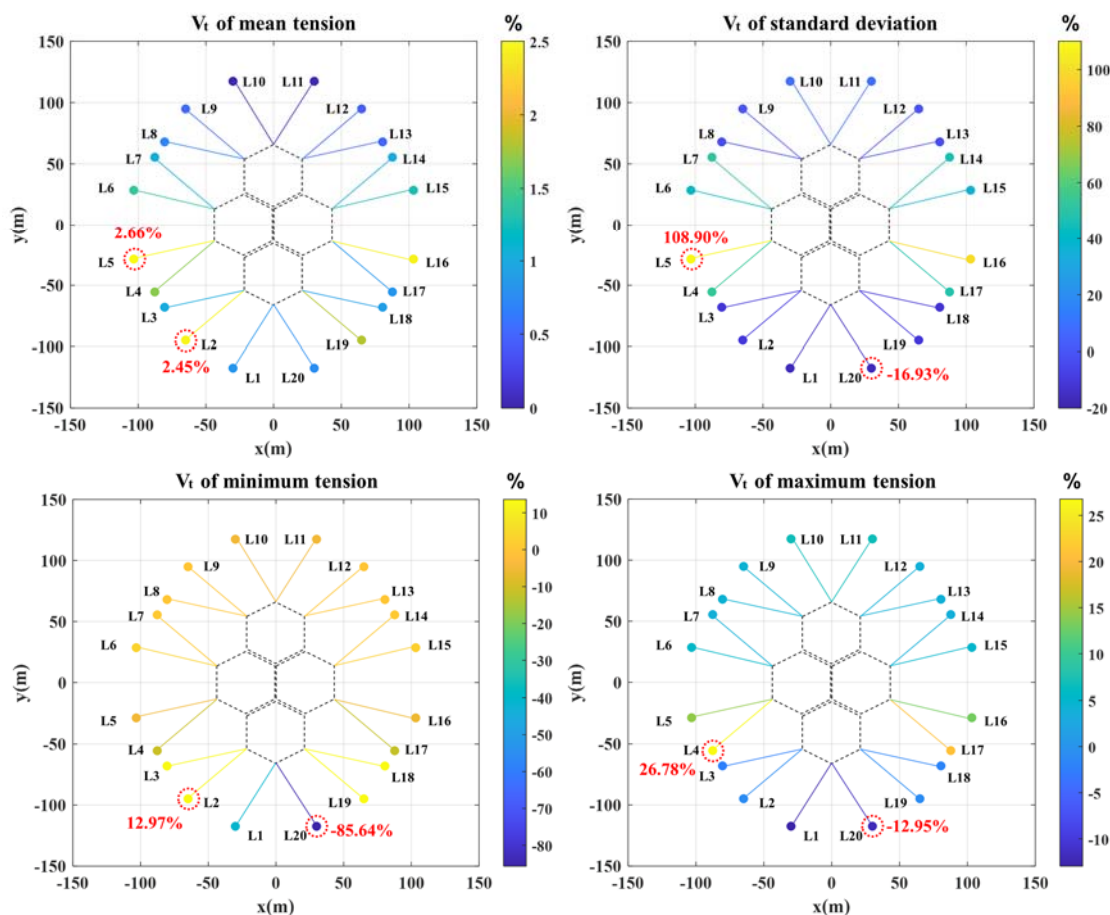| Line no.	1	2	3	4	5	6	7	8	9	10
Mean/kN	228.0	25.0	7.2	26.0	7.5	4.6	3.9	4.7	3.9	3.9
Std/kN	139.8	2.2	0.7	4.9	0.6	0.3	0.2	0.5	0.3	0.4
Min/kN	0.1	16.6	5.3	16.1	5.8	3.8	3.5	3.3	3.2	2.9
Max/kN	917.6	33.7	9.5	46.2	9.3	5.4	4.3	6.2	4.9	5.1
Line no.	11	12	13	14	15	16	17	18	19	20
Mean/kN	3.9	3.9	4.7	3.9	4.6	7.5	25.8	7.2	24.9	227.8
Std/kN	0.4	0.3	0.5	0.2	0.3	0.6	4.8	0.7	2.2	139.2
Min/kN	2.9	3.2	3.3	3.5	3.8	5.8	16.1	5.3	16.7	0.0
Max/kN	5.1	4.9	6.2	4.3	5.3	9.2	44.8	9.6	33.7	928.1

Fig. 12 Mooring tension Variation between multi-body and single-body analysis

Table 4 displays the statistical data of mooring line tension in the multi-body model, including the mean value, standard deviation (Std), minimum value (Min), and maximum value (Max). Results show that L1 and L20 play the main role when wind and waves are incident from 90 deg. The tension on these lines is much higher compared to other mooring lines. The mean, standard deviation, minimum, and maximum values of V_t for the two models can be seen in Fig. 12. The cloud chart illustrates that different

mooring lines are affected differently in the multi-body model, with lines experiencing higher tension generally exhibiting greater variations.

From the variations in each mooring line tension, it can be observed that there is an increase in mean tension across all mooring lines, though the variation is marginal, with a maximum difference of only 2.7%. This marginal is possibly due to the difference in the added mass on the surge. After considering the multi-module effect, the maximum, standard deviation, and minimum tension of L1 and L20 exhibit a more considerable reduction, reaching a maximum difference of 13.0%, 16.9% and 85.6%, respectively. On the contrary, the mooring lines connected to the platform #1 and #3 have a more substantial increase in tension response, with an increase of 26.8% of the maximum value. This might be attributed to the more pronounced increase in their surge and heave motion response duo to the weaker connection.

5.3 Effects of wave parameters

Wave height and wave period are essential parameters of the sea state [23]. In this subsection, the impact of multi-body interaction on FPV performance is analyzed under different wave parameters. Based on the Stokes 2nd order wave theory, a series of regular waves are selected with different wave periods or wave heights. A constant wind speed of 30 m/s is set in the simulation.
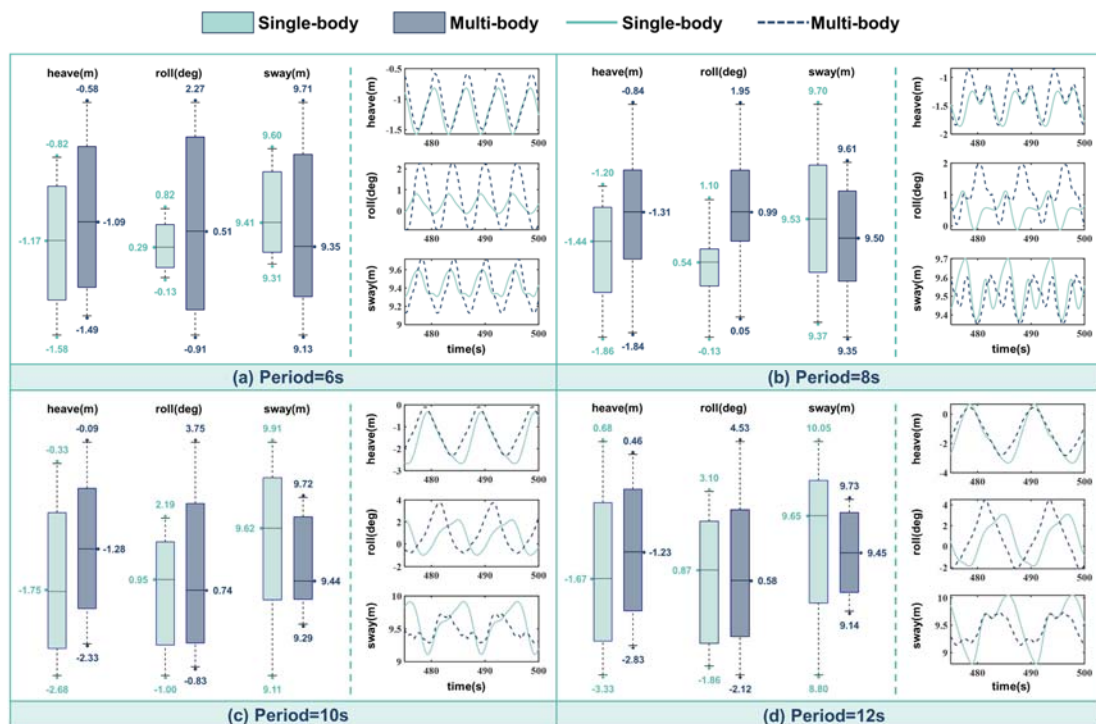
5.3.1 Effects of wave period

Fig. 13 The box diagrams and time histories of heave, roll, and sway under different wave periods

To explore the effects of wave periods, we chose a series of regular waves with a consistent wave height of 3 m and different periods of 6 s, 8 s, 10 s, and 12 s. The same wave elevation is used for the single-model and the multi-body model.

Fig. 13 shows the box diagrams as well as the time histories of heave, roll, and sway response comparisons. Compared with the single-body model, the motion trajectories in the multi-body model exhibit similar characteristics under the same wave impact, although multi-body interaction leads to changes in both the amplitude and phase angle of the motion.

For the heave motion, the equilibrium position is elevated after considering multi-body interaction under different wave periods. In the multi-body model, heave oscillations become more intense at shorter periods but diminish at periods of 10 s and 12 s compared to the single-body model. This is mainly because the wavelength is closer to the scale of the single-body model when the wave period approaches 11 s.

In terms of roll, the multi-body model increases the median trim angle under wave periods of 6 s and 8 s but reduces it under periods of 10 s and 12 s. Admittedly, the maximum roll response in the multi-body model consistently exceeds that of the single-body model, while this difference decreases as the wave period increases. Under 6 s period, the roll amplitudes are markedly larger in the multi-body model. The reason behind this phenomenon lies in the wavelength, which is closer to the scale of platform #2 in this case.

The sway motion experiences slight fluctuations in both models under different periods. In the single-body model, both the median and maximum sway responses consistently increase with longer periods and are larger than those in the multi-body model, except for the 6 s wave period. Specifically, under the 6 s period, the sway response is particularly significant, and the reason is similar to that discussed in roll.

It can be concluded from Fig. 13 (b) that the time histories of motion show different trajectories with double peaks under the 8 s wave period, indicating that a new frequency component appears in the motion response. This phenomenon occurs because the external excitation frequency is close to half of the natural frequency of roll and heave. A similar yet insignificant phenomenon can be observed in the sway under periods of 10 s and 12 s, demonstrating that sway exhibits sensitivity to multi-order frequencies.
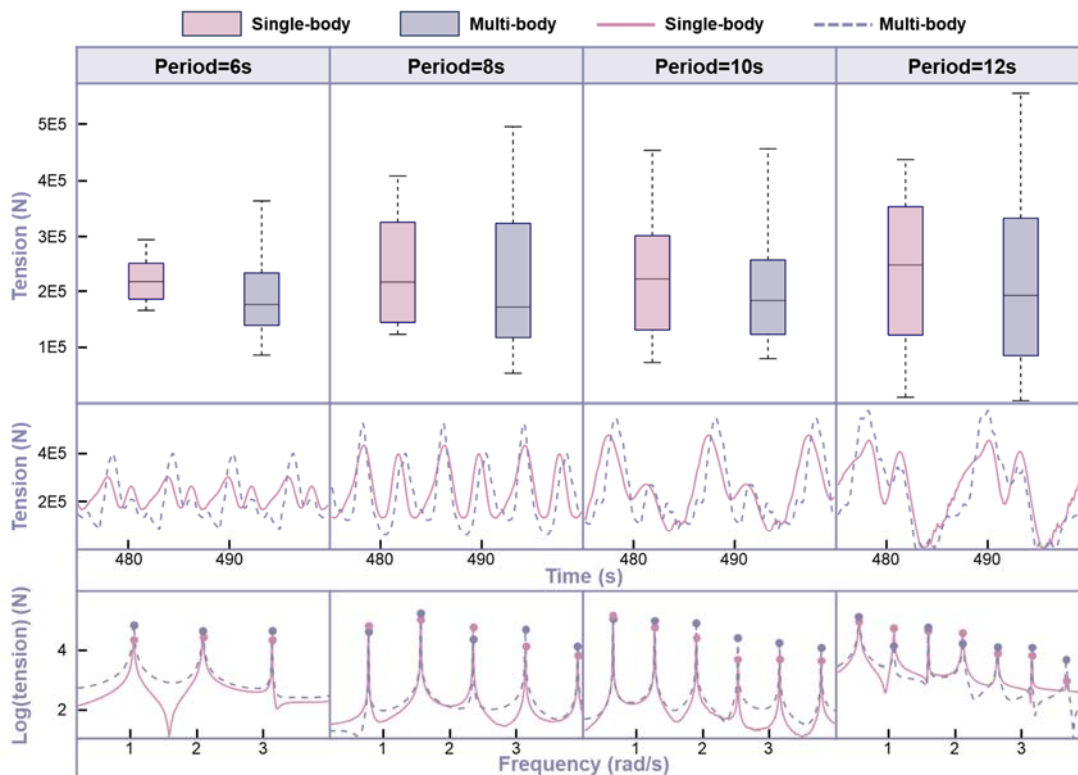
Fig. 14 The box diagrams, time histories and frequency response curves of tension in the L1

Fig. 14 displays the box diagrams, time histories, and frequency response curves of tension in L1, which is the most critical mooring line in platform #2. It is clear that the multi-body model reduces mean tension but exhibits more significant tension and more dramatic variation across most selected wave periods. Particularly, at the period of 10 s, the mooring line tension in the single-body model approaches that of the multi-body model. The phenomenon may be attributed to the fact that the wavelength closely matches the length of the whole floating system. Additionally, the mean tension in two models change slightly in these four cases, which means it is not sensitive to the wave period.

According to the frequency response curves, multi-order frequencies between the tension response frequencies and the encounter frequencies are clearly visible. We also find that there are higher amplitudes for multi-order frequency response when considering multi-body interaction, indicating stronger nonlinearity in the multi-body model. As discussed above, when the wave period approaches twice the natural period of heave and roll, the multi-body model tension response shows a prominent peak of double-order frequency, so that the time history of tension shows more substantial high-frequency characteristics. Moreover, the multi-order frequency characteristics of mooring line tension are more significant than those of motion in both the single-body model and the multi-body model.

5.3.2 Effects of wave height

The effects of wave height on motion and mooring response are discussed in this subsection. A series of regular waves are set with a wave period of 7 s and different heights of 1.5 m, 2.5 m, 3.5 m, and 4.5 m.
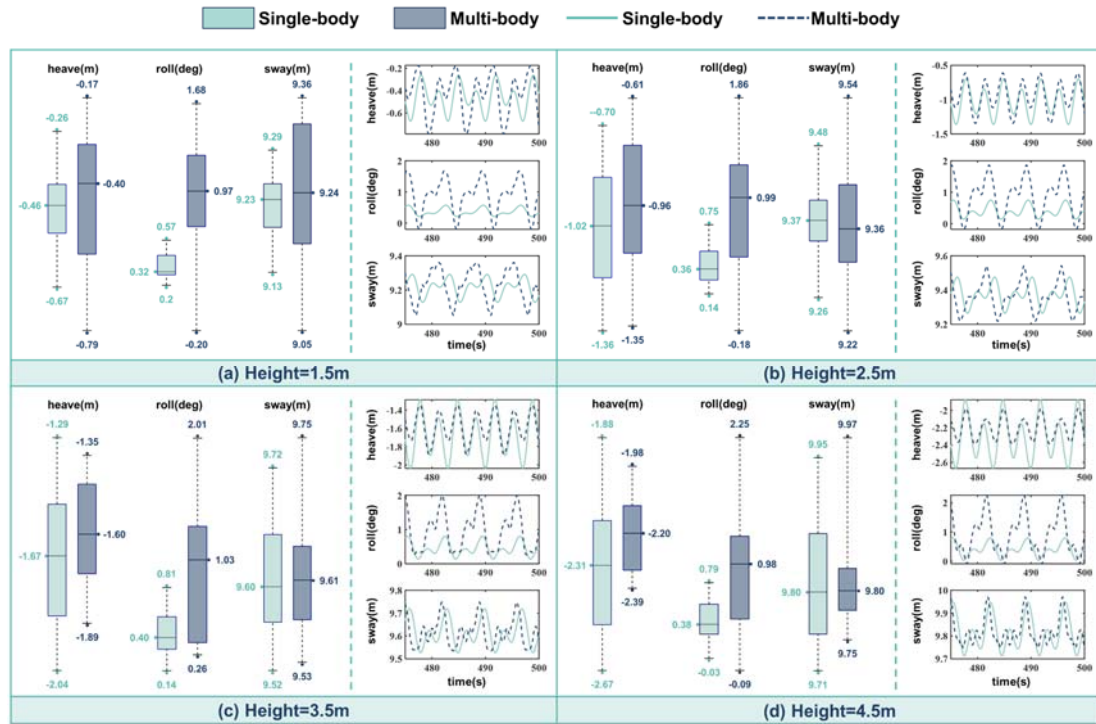

Fig. 15 The box diagrams and time histories of heave, roll, and sway under different wave heights

The box diagrams and time histories of heave, sway, and roll are shown in Fig. 15. It can be observed that wave height has a slight impact on the motion trajectory and frequency, whereas significantly influences the outcome of the multi-body and single-body models. The effects of multi-body interaction on roll do not vary significantly with increasing wave heights, and the roll in the multi-body model is remarkably more intense in all cases. However, the disparity in heave between the two models becomes more pronounced with the increasing wave height. Specifically, the heave of the multi-body model is much higher than that of the single-body model at a 1.5 m wave height, yet the discrepancy progressively diminishes with the increase in wave height, and even reverses at 3.5 m and 4.5 m wave heights. The results demonstrate that roll significantly varies between the two models under different wave heights, while the multi-body effect in heave is more sensitive to height.

According to the box diagrams of sway, the discrete degree of sway in the multi-body model decreases as wave heights increase, whereas it increases in the single-body model. In addition, sway in both models increases with higher wave heights. Although the median sway appears similar between the multi-body model and the single-body model, the maximum values are always larger when considering multi-body

23

interactions. The higher the wave height, the smaller this difference between the two models.
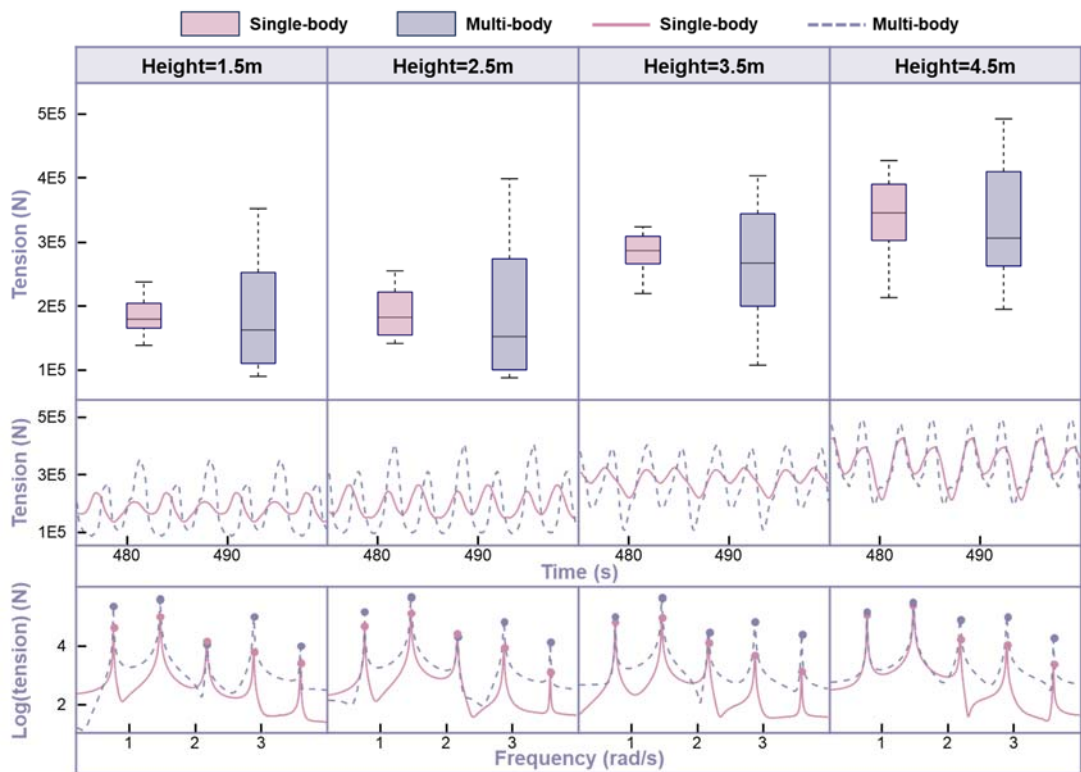

Fig. 16 The box diagrams, time histories and frequency response curves of tension in the L1

The box diagrams, time histories, and frequency response curves in tension of the L1 are shown in Fig. 16. According to the frequency response curves, the frequency component is insensitive to the wave heights, The multi-order frequencies, observed in all cases, are more significant in the multi-body model. Similar to the effects of wave periods, the mean tension in the single-body model is lower than that in the multi-body model. This difference may be due to variations in the added mass of surge. Moreover, the mooring line tension exhibits minimal variation at lower wave heights, while the disparity can be up to 39.4% when considering multi-body interaction. At a wave height of 4.5 m, the mooring tension of the two models are closer to each other, although the multi-body model mooring system faces greater risks under different wave heights.

6. Conclusion

In this paper, a hexagon-type floating photovoltaic is proposed and the dynamic coupled model is established in the time domain to investigate the multi-body effects. The influence of environmental load on multi-body interactions is also studied.

By comparing the multi-body model and single-body model, the module motion and mooring line tension exhibit different behavior. Under irregular wave conditions, sway appears to exhibit the least sensitivity to the multi-body interaction. However, roll

increases significantly, especially near the peak value. For heave response, there are slight changes in the upstream platform, but a vast difference in the middle platforms. For mooring tension, the mean values of mooring loads increase across all lines, while the maximum value of tension in the mooring system decreases.

Under regular wave conditions, multi-order frequencies are observed. As wave periods increase, the differences in roll between the two models gradually decrease, whereas the influence of the multi-body model on heave and sway exhibits an opposite trend compared to lower periods. On the other hand, the effect of multi-body interaction on roll is almost constant at different wave heights, while the effect on heave and sway is more sensitive. With the increasing wave height, the mooring tensions of the two models become closer.

In future work, it is essential to consider the effects of module arrangements and connection types on multi-body interactions. Furthermore, the safety of the floaters warrants further research on transient responses under more dangerous sea conditions. For example, freak waves are known for their destructiveness and unpredictability. Hence, a study of the FPV dynamic response under the crest of freak waves may be necessary [24,25,26]. Additionally, the effects of broken mooring lines are another potential issue [27]. In further work, line dynamics will be incorporate instead of the quasi-static method. Moreover, it is necessary to point out that the FPV structures are simplify as rigid bodies in the current work, but this conflicts with their flexible nature. To address this issue, hydroelasticity theory will be introduced in our future work, such as modal analysis method [28] and the beam-connected-discrete modules method (BCDM) method [29]. The analytical method can provide a more comprehensive assessment of floating PV system performance.

Acknowledgement

References

[1] Li, Y., Li, H., Wang, Z., Li, Y., Wang, B., & Tang, Y. (2023). The dynamic response of a Spar-type floating wind turbine under freak waves with different properties. Marine

Structures, 91, 103471.

[2] Ranjbaran, P., Yousefi, H., Gharehpetian, G. B., & Astaraei, F. R. (2019). A review on floating photovoltaic (FPV) power generation units. Renewable and Sustainable Energy Reviews, 110, 332-347.

[3] Olkkonen, V., Haaskjold, K., Klyve, Ø. S., & Skartlien, R. (2023). Techno-economic feasibility of hybrid hydro-FPV systems in Sub-Saharan Africa under different market conditions. Renewable Energy, 215, 118981.

[4] Crijns-Graus, W., Wild, P., Amineh, M. P., Hu, J., & Yue, H. (2022). International comparison of research and investments in new renewable electricity technologies: A focus on the European union and China. Energies, 15(17), 6383.

[5] Ramanan, C. J., Lim, K. H., Kurnia, J. C., Roy, S., Bora, B. J., & Medhi, B. J. (2024). Towards sustainable power generation: Recent advancements in floating photovoltaic technologies. Renewable and Sustainable Energy Reviews, 194, 114322.

[6] Shi, W., Yan, C., Ren, Z., Yuan, Z., Liu, Y., Zheng, S., ... & Han, X. (2023). Review on the development of marine floating photovoltaic systems. Ocean Engineering, 286, 115560.

[7] Du, J., Zhang, D., Zhang, Y., Xu, K., Chang, A., & Zhao, S. (2024). Design and comparative analysis of alternative mooring systems for offshore floating photovoltaics arrays in ultra-shallow water with significant tidal range. Ocean Engineering, 302, 117649.

[8] Song, J., Kim, J., Chung, W. C., Jung, D., Kang, Y. J., & Kim, S. (2023). Wave-induced structural response analysis of the supporting frames for multiconnected offshore floating photovoltaic units installed in the inner harbor. Ocean Engineering, 271, 113812.

[9] Song, J., Kim, J., Lee, J., Kim, S., & Chung, W. (2022). Dynamic response of multiconnected floating solar panel systems with vertical cylinders. Journal of Marine Science and Engineering, 10(2), 189.

[10] Yan, C., Shi, W., Han, X., Li, X., & Verma, A. S. (2023). Assessing the dynamic behavior of multiconnected offshore floating photovoltaic systems under combined wave-wind loads: A comprehensive numerical analysis. Sustainable Horizons, 8, 100072.

[11] Ji, C., Gao, X., & Xu, S. (2024). Study on the influence of connector designs on the hydrodynamic performance of an offshore floating photovoltaic. Ocean Engineering, 308, 118298.

[12] Ramanan, C. J., Lim, K. H., Kurnia, J. C., Roy, S., Bora, B. J., & Medhi, B. J. (2024). Design study on the parameters influencing the performance of floating solar PV. Renewable Energy, 223, 120064.

[13] Tina, G. M., Scavo, F. B., Merlo, L., & Bizzarri, F. (2021). Analysis of water

environment on the performances of floating photovoltaic plants. Renewable Energy, 175, 281-295.

[14] Ikhennicheu, M., Danglade, B., Pascal, R., Arramounet, V., Trébaol, Q., & Gorintin, F. (2021). Analytical method for loads determination on floating solar farms in three typical environments. Solar Energy, 219, 34-41.

[15] Oliveira-Pinto, S., & Stokkermans, J. (2020, December). Marine floating solar plants: An overview of potential, challenges and feasibility. In Proceedings of the Institution of Civil Engineers-Maritime Engineering (Vol. 173, No. 4, pp. 120-135). Thomas Telford Ltd.

[16] Wang, B., Li, Y., Huang, L., Yao, Y., & Qin, Y. (2024). Dynamic analysis of a novel star-type floating photovoltaic system with flexible connectors. Ocean Engineering, 304, 117854.

[17] Claus, R., & López, M. (2023). A methodology to assess the dynamic response and the structural performance of floating photovoltaic systems. Solar Energy, 262, 111826.

[18] Liu, Y., Ren, N., & Ou, J. (2022). Hydrodynamic analysis of a hybrid modular floating structure system under different wave directions. Applied Ocean Research, 126, 103264.

[19] Jiang, Z., Dai, J., Saettone, S., Tørå, G., He, Z., Bashir, M., & Souto-Iglesias, A. (2023). Design and model test of a soft-connected lattice-structured floating solar photovoltaic concept for harsh offshore conditions. Marine Structures, 90, 103426.

[20] Dai, J., Zhang, C., Lim, H. V., Ang, K. K., Qian, X., Wong, J. L. H., ... & Wang, C. L. (2020). Design and construction of floating modular photovoltaic system for water reservoirs. Energy, 191, 116549.

[21] Clément, C., Bozonnet, P., Vinay, G., Pagnier, P., Nadal, A. B., & Réveillon, J. (2022). Evaluation of Morison approach with CFD modelling on a surface-piercing cylinder towards the investigation of FOWT Hydrodynamics. Ocean Engineering, 251, 111042.

[22] Koo, B. J., & Kim, M. H. (2005). Hydrodynamic interactions and relative motions of two floating platforms with mooring lines in side-by-side offloading operation. Applied Ocean Research, 27(6), 292-310.

[23] Hildeman, A., Bolin, D., & Rychlik, I. (2022). Joint spatial modeling of significant wave height and wave period using the SPDE approach. Probabilistic Engineering Mechanics, 68, 103203.

[24] Li, H., Li, Y., Li, G., Zhu, Q., Wang, B., & Tang, Y. (2024). Transient tower and blade deformations of a Spar-type floating wind turbine in freak waves. Ocean Engineering, 294, 116801.

[25] Li, Y., Qu, X., Liu, L., Xie, P., Yin, T., & Tang, Y. (2020). A numerical prediction on the transient response of a spar-type floating offshore wind turbine in freak waves.

Journal of Offshore Mechanics and Arctic Engineering, 142(6).

[26] Qu, X., Li, Y., Tang, Y., Hu, Z., Zhang, P., & Yin, T. (2020). Dynamic response of spar-type floating offshore wind turbine in freak wave considering the wave-current interaction effect. Applied Ocean Research, 100, 102178.

[27] Li, Y., Zhu, Q., Liu, L., & Tang, Y. (2018). Transient response of a SPAR-type floating offshore wind turbine with fractured mooring lines. Renewable Energy, 122, 576-588.

[28] Zhang, Y., Zhang, X., Chen, Y., Tian, X., & Li, X. (2024). A frequency-domain hydroelastic analysis of a membrane-based offshore floating photovoltaic platform in regular waves. Journal of Fluids and Structures, 127, 104125.

[29] Shi, Y., Wei, Y., Tay, Z. Y., & Chen, Z. (2023). Hydroelastic analysis of offshore floating photovoltaic based on frequency-domain model. Ocean Engineering, 289, 116213.